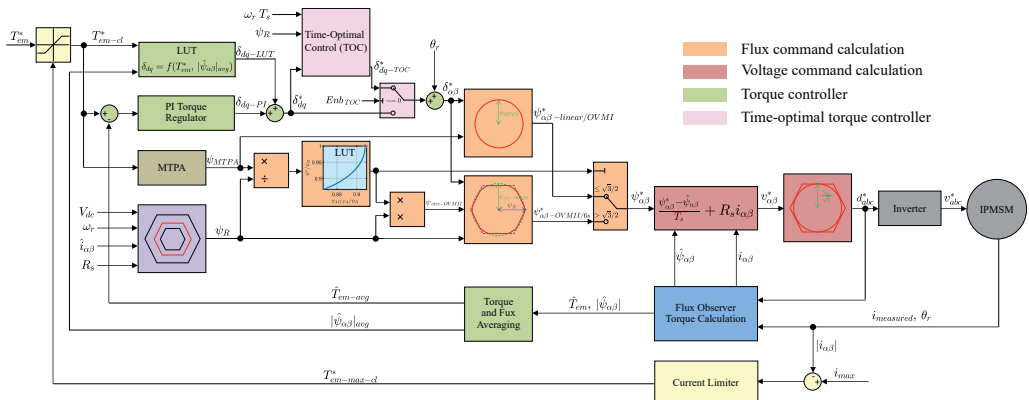


Forschungsberichte Elektrische Antriebstechnik und Aktorik

Hrsg.: Prof. Dr.-Ing. Dieter Gerling

Hadi El Khatib

Deadbeat Flux and Torque Control in the Linear, Overmodulation, and Six-Step Regions for Automotive Traction Applications



Deadbeat Flux and Torque Control in the Linear, Overmodulation, and Six-Step Regions for Automotive Traction Applications

Hadi El Khatib

Vollständiger Abdruck der von der Fakultät für Elektro- und Informationstechnik der Universität der Bundeswehr München zur Erlangung des akademischen Grades eines

Doktor-Ingenieurs (Dr.-Ing.)

genehmigte Dissertation.

Prüfungsvorsitzender:

Prof. Dr.-Ing. habil. Thomas Weyh

Gutachter:

1. Prof. Dr.-Ing. Dieter Gerling
2. Prof. Dr.-Ing. Joachim Böcker

Die Dissertation wurde am 5.12.2022 bei der Universität der Bundeswehr München eingereicht und durch die Fakultät für Elektro- und Informationstechnik am 25.5.2023 angenommen. Die mündliche Prüfung fand am 15.9.2023 statt.

Forschungsberichte Elektrische Antriebstechnik und Aktorik

Band 54

Hadi El Khatib

**Deadbeat Flux and Torque Control in the Linear,
Overmodulation, and Six-Step Regions for
Automotive Traction Applications**

Shaker Verlag
Düren 2023

Bibliographic information published by the Deutsche Nationalbibliothek

The Deutsche Nationalbibliothek lists this publication in the Deutsche Nationalbibliografie; detailed bibliographic data are available in the Internet at <http://dnb.d-nb.de>.

Zugl.: München, Univ. der Bundeswehr, Diss., 2023

Copyright Shaker Verlag 2023

All rights reserved. No part of this publication may be reproduced, stored in a retrieval system, or transmitted, in any form or by any means, electronic, mechanical, photocopying, recording or otherwise, without the prior permission of the publishers.

Printed in Germany.

ISBN 978-3-8440-9319-3

ISSN 1863-0707

Shaker Verlag GmbH • Am Langen Graben 15a • 52353 Düren

Phone: 0049/2421/99011-0 • Telefax: 0049/2421/99011-9

Internet: www.shaker.de • e-mail: info@shaker.de

Abstract

Six-step modulation offers notable advantages over the conventional Space Vector Pulse Width Modulation (SVPWM) in the flux-weakening region. It enhances the torque capability of the machine and guarantees maximum power performance by maximizing battery voltage utilization, a critical component of electric cars due to its high cost. Moreover, the system's efficiency is enhanced by reducing the phase current required for flux weakening and minimizing switching losses. Conversely, under identical operational requirements, it becomes feasible to downsize the battery capacity and/or machine/inverter ratings, leading to cost, weight, and space savings.

This thesis introduces an enhanced Deadbeat Flux Vector Controller (DBFC) as a one single control law capable of operating interior permanent magnet synchronous machines (IPMSMs) across the entire torque-speed range. Stable operation in the full voltage modulation range, including SVPWM, overmodulation (I and II), and six-step, is achieved through precise tracking of various flux trajectories. DBFC enables a continuous and seamless transition between the different operating regions, with the modulation index varying linearly with speed in the constant torque region. With this proposed strategy, undesirable torque dynamics, stability problems, and increased computational efforts, associated with using multiple control laws are completely avoided.

A comprehensive analysis of DBFC's transient performance at the maximum voltage limit (six-step) is conducted. A time-optimal torque control algorithm is developed to achieve the fastest possible torque response, significantly reducing the settling time, particularly when operating at the voltage limit (six-step). The torque can be controlled with high accuracy and high robustness to machine parameter variations. DBFC allows for the control of the instantaneous flux vector, encompassing both steady-state and transient flux trajectories, without requiring trade-offs between steady-state six-step behavior and excellent transient performance. The proposed controller offers significant advantages over conventional Field-Oriented Control (FOC) and it is simpler to implement.

If operation in overmodulation, including six-step, is not desirable based on the application and requirements, another variant of the classical Direct Torque Controller (DTC) can be employed. The operation of the Deadbeat-Direct Torque and Flux Controller (DB-DTFC) is extended to the second flux weakening region by the Square-Root Condition (SRC), ensuring robust and reliable maximum-torque-per-flux (MTPF) operation with a circular flux trajectory. A robust Gopinath flux linkage observer is implemented and evaluated since the flux is a controlled variable for both DBFC and DB-DTFC.

Simulation and experimental results are provided to validate the proposed control strategies, which have been implemented on an automotive microcontroller with a high-power, high-performance automotive traction machine.

Acknowledgment

First and foremost, I am extremely grateful to Audi AG for funding this project and to the Bundeswehr University Munich for providing an exceptional research environment.

I would like to express my sincere gratitude to Prof. Dr.-Ing. Dieter Gerling for offering me this great research opportunity. In addition to the guidance, continuous support, and sage advice, Professor Gerling granted me the autonomy to explore and implement my own ideas throughout the research project. I would also like to express my deepest appreciation to Prof. Dr.-Ing. Joachim Böcker for being the second examiner of this thesis and for the insightful comments and suggestions.

I am deeply indebted to Dr.-Ing. Michael Saur whose inspiration led me into the realm of control of electric drives. I had the pleasure of working with him for more than three years. He provided invaluable support that helped guide this entire project. Without him, I would not have been able to complete this research.

I extend my thanks to Dr.-Ing. Benjamin Grothmann for reviewing this thesis and for his support in extending the PhD project. Special thanks to Dr. Daniel Gaona for motivating me at the beginning of my PhD project and for the valuable and fruitful discussions. Thanks should also go to Emebet Gebeyehu Gedlu, Mario peña, and Gerardo Pantoja for the great teamwork and the wonderful time at Audi. I would like to extend my sincere thanks to Dr.-Ing. Andreas Joerg, Nils Conzelmann, Martin Adam, and all the Audi colleagues for the invaluable collaboration.

Many thanks to Dr.-Ing. Johann Mayer. The door to his office was always open whenever I needed help. I also thank Dr.-Ing. Harald Hofmann and the rest of the EAA colleagues at the Bundeswehr University Munich for their support.

Words cannot express my gratitude to my parents, my sisters, my future wife Afnan, and the rest of my family for their unconditional love and support. I owe you everything.

Contents

Abstract	i
Acknowledgment	iii
List of Figures	ix
List of Tables	xvi
Nomenclature	xvii
1 Introduction	1
1.1 Motivation	1
1.2 Thesis Outline	3
2 State-of-the-Art Review	5
2.1 Interior Permanent Magnet Synchronous Machines Model	5
2.1.1 Reference Frame Theory	5
2.1.2 IPMSM Model	5
2.2 Machine and Inverter Losses	7
2.3 Machine and Inverter Limits	8
2.4 Operating Regions of IPMSMs	9
2.4.1 Constant Torque Region	11
2.4.2 Flux Weakening Region I (FW I)	11
2.4.3 Flux Weakening Region II (FW II)	12
2.4.4 Capability Curve of IPMSMs	12
2.5 Machine Parameter Variations	13
2.5.1 Winding Resistance	13
2.5.2 Magnetic Model	13
2.6 Current and Flux Linkage Observers	14
2.6.1 Discrete-Time Luenberger Stator Current Observer	14
2.6.2 Discrete-Time Gopinath Stator Flux Linkage Observer	15
2.7 Three-Phase Voltage Source Inverter	17
2.7.1 Modelling of a Three-Phase Voltage Source Inverter	17
2.7.2 Inverter's Switching Devices	19
2.7.3 Inverter Nonlinearities	20

2.8	Modulation Strategies for the Three-Phase Inverters	22
2.8.1	Six-Step Modulation	22
2.8.2	Pulse Width Modulation	24
2.8.2.1	Programmed PWM technique [1, 2]	25
2.8.2.2	Carrier-Based PWM technique [3]	25
2.8.2.3	Space Vector Pulse Width Modulation (SVPWM) [4]	25
2.9	Operating Regions of the Inverter	27
2.9.1	Overmodulation region I (OVM I), $1 \leq MI < 1.05$	29
2.9.2	Overmodulation region II (OVM II), $1.05 \leq MI < 1.103$	29
2.10	Control Strategies for IPMSMs in the Overmodulation Region and Six-Step	31
2.10.1	Voltage Angle Torque Control (VATC)	31
2.10.2	Current Vector Control (CVC)	32
2.10.3	Direct Self-Control (DSC)	32
2.10.4	Stator Flux-Based Space Vector Modulation	34
2.10.5	Deadbeat-Direct Torque and Flux Control	34
2.10.5.1	Analytical Solution of DB-DTFC	35
2.10.5.2	Graphical Solution of DB-DTFC	37
2.10.5.3	DB-DTFC in the Overmodulation Region	37
2.10.6	Deadbeat Flux Vector Control (DBFC)	37
2.11	Research Opportunities	38
3	Extended Deadbeat-Direct Torque and Flux Control Law	41
3.1	Operating in FW I and FW II	42
3.2	DB-DTFC and SRC Algorithms	43
3.2.1	DB-DTFC Algorithm	43
3.2.2	SRC Algorithm	44
3.2.3	Implementation of DB-DTFC with SRC	46
3.2.3.1	Flux and Current Observers	46
3.2.3.2	Current Limiter	47
3.3	Simplified DB-DTFC	47
3.4	Simulation Results	49
3.4.1	Transient Response of DB-DTFC in the MTPF Region	49
3.4.2	Parameter Sensitivity Analysis of DB-DTFC and CVC in FW II	51
3.4.3	Effect of Iron Loss on the MTPF Operation	53
3.5	Experimental Results	55
3.5.1	Testbench A (dSPACE)	55
3.5.2	Testbench B (Automotive Microcontroller)	57
3.5.2.1	Sensitivity of DB-DTFC and CVC to changes in ψ_{pm}	57
3.5.2.2	Operation at the Current Limit	59
3.5.2.3	Limitation of SRC Due to Flux Estimation Accuracy	60
3.6	Conclusions	61
4	Implementation and Evaluation of a Robust Gopinath Flux Linkage Observer	63
4.1	Introduction	63

4.2	Sensitivity Analysis of the Current Model	64
4.2.1	Effect of Machine Parameter Variations	65
4.2.2	Effect of Iron Loss	65
4.3	Sensitivity Analysis of the Voltage Model	68
4.3.1	Effect of Stator Resistance Variation	68
4.3.2	Effect of Discretization Errors	69
4.3.3	Effect of Deadtime and Switching Device Voltage Drop	71
4.4	Factors Affecting the Gopinath Model	73
4.4.1	Encoder Offset Misalignment	73
4.4.2	Selection of the FO Bandwidth	75
4.5	Validation of the Flux Observer's Estimation Accuracy Using SRC	75
4.6	Conclusions	76
5	Development of a Deadbeat Flux Vector Control Strategy for the Complete Operating Range	79
5.1	Identification of Reference Flux Trajectories for the Linear, OVM, and Six-step Regions	81
5.1.1	Flux Trajectory in the Linear Region	82
5.1.2	Flux Trajectory in the Six-Step Mode	82
5.1.3	Flux Trajectories in the Overmodulation Region	84
5.1.3.1	Flux Trajectory in OVM I	84
5.1.3.2	Flux Trajectory in OVM II	85
5.1.4	Flux Trajectories with Synchronous PWM	86
5.2	Torque Control and Reference Flux Angle Calculation	87
5.2.1	Open-Loop Solution	87
5.2.2	Closed-Loop Solution	89
5.2.3	Hybrid Solution	89
5.3	Transition Between the Different Operating Regions	90
5.3.1	Determination of the Feasible Flux Trajectories	90
5.3.2	Achieving a Linear Change in Modulation Index in OVM II	92
5.4	Voltage Selection and Modulation for Six-Step Operation	93
5.4.1	Volt-sec Commands at the Flux Hexagon's Edges	93
5.4.2	Volt-sec Commands at the Flux Hexagon's Corners	95
5.5	Proposed DBFC Control Scheme	96
5.6	Simulation Results	98
5.6.1	DBFC in the Linear Voltage Region	98
5.6.2	Tracking of the Different Flux Trajectories	98
5.6.3	Torque Control	100
5.7	Experimental Results	101
5.7.1	Hardware-in-the-Loop Testbench	102
5.7.1.1	Test 1: Experimental Evaluation of DBFC for a Wide Operating Speed Range	102
5.7.1.2	Test 2: Experimental Evaluation of the Torque Controller Using the Feedforward Method	103
5.7.2	Automotive Testbench with a Traction Machine	105

5.7.2.1	Test 1: Experimental Evaluation of Continuous Transition from the Linear Region to Six-Step	105
5.7.2.2	Test 2: Experimental Evaluation of the Current Harmonics in Six-Step	108
5.7.2.3	Test 3: Experimental Evaluation of the Torque Controller Using the Hybrid Method	109
5.8	Conclusions	111
6	Development of a Time-Optimal Torque Control Strategy for DBFC	113
6.1	Unoptimized Flux Trajectory in the Transient State	114
6.2	Time-Optimal Torque Control with DBFC	116
6.3	Relative Size of the Flux Hexagon and the Volt-sec Hexagon	122
6.4	Determining the Optimal Number of Steps for TOC	123
6.5	Experimental Results	125
6.5.1	Torque Transient at Low Speeds	125
6.5.1.1	$T_{em}^* = 0.20 \rightarrow 0.51 \text{ p.u.}$, $n_{rm} = 0.47 \text{ p.u.}$	125
6.5.1.2	$T_{em}^* = 0 \rightarrow 0.20 \text{ p.u.}$, $n_{rm} = 0.47 \text{ p.u.}$	128
6.5.2	Torque Transient at High Speeds	130
6.5.2.1	$T_{em}^* = 0 \rightarrow 0.43 \text{ p.u.}$, $n_{rm} = 0.71 \text{ p.u.}$	130
6.5.2.2	$T_{em}^* = 0 \rightarrow 0.27 \text{ p.u.}$, $n_{rm} = 1 \text{ p.u.}$	130
6.6	Conclusions	130
7	Conclusions and Recommended Future Work	135
7.1	Conclusions	135
7.2	Recommended Future Work	138
A	Comparison Between DBFC and DB-DTFC	141
B	List of Publications	143
B.1	Journal Papers	143
B.2	Conference Papers	143
	Bibliography	145

List of Figures

1.1	World greenhouse gas emissions by sector in 2019 [5].	2
1.2	Basic components of the electric traction drive systems.	3
2.1	Definition of the different reference frames.	6
2.2	Electromagnetic torque and reluctance torque for different synchronous machine constructions [6].	6
2.3	Two-phase equivalent circuit of IPMSMs considering iron losses. Left: $d - axis$. Right: $q - axis$	7
2.4	Current limit, voltage limit, and torque hyperbolas of IPMSMs in the current, flux, and voltage planes. (a)-(c): constant speed and increasing torque. (d)-(f): constant torque and increasing speed.	9
2.5	Produced torque for variable $i_d - i_q$ combinations. (a): constant current magnitude. (b): constant flux magnitude.	10
2.6	MTPA and MTPF trajectories for IPMSMs in the current plane.	11
2.7	Different possibilities which exist at the point where the MTPF trajectory intersects with the current-limit circle.	12
2.8	Capability curve of an IPMSM with flux weakening operation considering the voltage and current constraints.	13
2.9	Block diagram of the discrete-time Luenberger current observer in the synchronous reference frame (f_{dq}) for IPMSMs.	15
2.10	Block diagram of the discrete-time Gopinath stator flux linkage observer. Current model (green) in the synchronous reference frame (f_{dq}). Voltage model (blue) in the stationary reference frame ($f_{\alpha\beta}$). PI regulator (orange). One-step delay in the feedback path (yellow) [7].	17
2.11	Bode diagram of the flux observer's controller (Bandwidth = 50 Hz). . . .	17
2.12	Three-phase voltage source inverter circuit.	18
2.13	$v - i$ characteristics and symbols of the MOSFET [(a), (c)] and the IGBT [(b), (d)].	20
2.14	Pole-voltage waveform distortion due to the inverter nonlinearities (dead-time, turn-on and turn-off time delays, voltage drop across the switches and the diodes). (a) and (c): positive phase current. (b) and (d): negative phase current.	21
2.15	Inverter's output voltages in the six-step mode.	23

2.16	Phase voltage (v_{as}) and line voltage (v_{ab}) harmonic components (up to the 17 th order) plotted in the time and frequency domains.	24
2.17	Space vector representation of the eight possible switching states for the three-phase inverter.	26
2.18	Basic concept of the SVPWM modulation. The voltage command (black) can be represented by a geometric summation of space vectors.	27
2.19	Locus of the voltage vector for an operation in (a): the linear region, (b): overmodulation, (c): six-step. (d) = (a) \cup (b) \cup (c) [8].	28
2.20	Different voltage modulation ranges [8].	28
2.21	Deference voltage adjustment in the overmodulation region.	29
2.22	Reference voltage adjustment (blue) in OVM I to achieve a linear change in MI	30
2.23	The holding angle of the voltage vector as a function of the desired modulation index in OVM II.	31
2.24	Reference voltage adjustment by the holding angle at eight distinct operating points in OVM II.	31
2.25	Block diagram of the direct self-controller [9].	33
2.26	Block diagram of the state-of-the-art DBFC.	38
3.1	Graphical interpretation of the DB-DTFC voltage solution for (a): $\Delta > 0$, (b): $\Delta = 0$, (c): $\Delta < 0$	45
3.2	Block diagram of the DB-DTFC algorithm showing the flux circle variables (blue), the differential torque line variables (green), the SRC (yellow), and the voltage command calculation (red).	46
3.3	Simulation results showing the graphical interpretation of the transient response applying DB-DTFC for an infeasible step command in torque ($T_{em}^* > T_{em-MTPF}$) at t_1 . The speed is 14000 min^{-1} , $ \psi_{dq} ^* = 0.06 \text{ Vs}$. $T_s = 100 \mu\text{s}$. Infeasible differential torque line (yellow). Differential torque line (red). Zero-change-in-torque line (grey) [10].	50
3.4	Simulation results showing the torque step response in FW II at 14000 min^{-1} ($T_{em}^* > T_{em-MTPF}$) [10].	51
3.5	Block diagram of the implemented hybrid flux weakening strategy for CVC in the second flux weakening region [10].	51
3.6	Simulation results showing the torque production using CVC and SRC (DB-DTFC) at two different temperatures (20°C and 120°C). The speed is 17000 min^{-1} . The flux command is $ \psi_{dq} = 0.045 \text{ Vs}$. The maximum torque command is applied [10].	52
3.7	Simulation results showing the torque production at 12000 min^{-1} and 17000 min^{-1} applying the CVC and the SRC solutions in FW II for detuned parameters in the machine model. (a) ψ_{pm} . (b) L_d . (c) L_q [10].	53
3.8	Block diagram of the experimental setup in Testbench A [10].	56
3.9	Experimental results showing the torque step response for an infeasible command ($T_{em}^* = 50 \text{ Nm}$) in FW II. $T_{em-MTPF} = 42 \text{ Nm}$, $n_{rm} = 6000 \text{ min}^{-1}$, $ \psi_{dq} = 0.01 \text{ Vs}$. $T_s = 100 \mu\text{s}$ [10].	56

3.10	Experimental results in FW II for a constant torque command and decreasing flux ($ \psi_{dq} ^* = 0.5 \rightarrow 0 \text{ Vs}$) at 6000 min^{-1} . (a)-(c): $T_{em}^* = 100 \text{ Nm}$. (d): $T_{em}^* = 150, 200 \text{ Nm}$ [10].	57
3.11	Experimental results showing the transition from CVC to closed-loop DB-DTFC (with SRC) in FW II at 17000 min^{-1} . The maximum modulation index is 1.05. $\psi_{pm} = 0.98 \hat{\psi}_{pm}$ [10].	58
3.12	Experimental results showing an operation at the current limit in FW II. The speed is 17000 min^{-1}	59
3.13	Experimental results showing the DB-DTFC operation at the current limit for a step increase in torque ($T_{em}^* = 0 \rightarrow 150 \text{ Nm}$). $ i_{dq} _{lim} = 150 \text{ A}$. (a) and (c): $K_p = 0, K_i = 5$. (b) and (d): $K_p = 0.06, K_i = 400$	60
3.14	Experimental results showing the torque dependency on the estimated flux angle in FW II at 17000 min^{-1} . $T_s = 100 \mu\text{s}$ [10].	60
4.1	Electromagnetic torque for different $i_d - i_q$ combinations at a constant flux magnitude ($ \psi_{dq} = 0.05 \text{ Vs}$) [11].	64
4.2	Simulation and experimental results showing the estimated and measured torque for a speed ramp from standstill to 9000 min^{-1} . The machine parameters ($\hat{L}_d, \hat{L}_q, \hat{\psi}_{pm}$) are intentionally detuned by $\pm 30\%$. The flux observer bandwidth is 100 Hz ($\sim 2000 \text{ min}^{-1}$). (a)-(b): CVC ($i_d^* = -190 \text{ A}, i_q^* = 110 \text{ A}$), the flux observer is in open-loop. (c): DB-DTFC ($T_{em}^* = 100 \text{ Nm}$), the flux observer is in closed-loop [11].	66
4.3	(a): dq -equivalent circuits for IPMSMs. (b), (c) and (d): estimated torque, flux magnitude, and flux angle errors caused by the iron loss. The current model is used for flux estimation and torque calculation [11].	67
4.4	Simulation results showing the torque, flux magnitude, and flux angle in the machine for a correct [(a)-(c)] and wrong [(d)-(f)] stator resistance estimation. The errors between ① and ② are shown in the third row [(g)-(i)].	69
4.5	Block diagram of the employed discrete-time Gopinath stator flux linkage observer. It includes the voltage phase correction (yellow), the inverter model (purple), the iron loss model (cyan), and the machine magnetic model (red). DB-DTFC & SRC/ DBFC algorithms (pink). Luenberger current observer (tan). The inverter and IPMSM (gray) [11].	70
4.6	Simulation results showing the estimated torque in FW II, applying the SRC, for different speed-dependent voltage offset-angles. The speed is 17000 min^{-1} . The maximum point (black cross) corresponds to the optimal setting [11].	70
4.7	Experimental results showing the estimated flux (a) and torque (b) for a speed ramp from 0 to 17000 min^{-1} . $T_{em}^* = 100 \text{ Nm}$ and $ \psi_{dq} ^* = 0.101 \text{ Vs}$ [11].	71
4.8	Experimental results showing the estimated torque (blue) in the MTPF region at the operating points in Table 4.2. The deadtime compensation value (red) is increased from $0 \mu\text{s}$ to $3 \mu\text{s}$. The speed is 1000 min^{-1} . The flux observer bandwidth is 5 Hz (100 min^{-1}). The filtered torque is shown as a dotted line [11].	73

4.9	Simulation results showing the (a) torque, (b) ψ_d , and (c) ψ_q for a variable d -axis current command normalized to the characteristic current (i_d^*/i_{cc}). The q -axis current command is set to zero ($i_q^* = 0 A$).	74
4.10	The torque-speed plane divided into six regions of operation.	75
4.11	Experimental results showing the torque dependency on the intentionally detuned flux angle in FW II at $17000 min^{-1}$. The operation is at the voltage limit in the linear region [11].	76
5.1	(a) Capability curve of IPMSMs with flux weakening (linear, OVM I, OVM II, six-step). The transition to six-step with (b) continuous and (c) discontinuous change in the modulation index. (d) Only the MTPA-flux can achieve maximum torque production at the current limit [12].	80
5.2	Flux trajectory (blue) for an arbitrary change in the commanded volt-sec vector (red) in the volt-sec plane (stationary reference frame) [8].	81
5.3	Flux setpoint as a function of the desired torque for MTPA operation, and its cubic function approximation [8].	82
5.4	Relative size of the volt-sec hexagon and the flux hexagon in the volt-sec plane (stationary reference frame). In this example, $R_s = 0 \Omega$ and $\frac{2\pi/6}{\omega_r T_s} = 4$ [8].	83
5.5	Effect of the stator resistance on the flux hexagon. In this example, $R_s \neq 0 \Omega$ and $\frac{2\pi/6}{\omega_r T_s} = 4$ [8].	83
5.6	The volt-sec and flux trajectories at the lower and upper boundaries of OVM I. In this example, $\frac{2\pi/6}{\omega_r T_s} = 4$ [8].	84
5.7	The minimum-flux-phase-error method applied to the flux trajectory. The flux angle is unchanged, the flux magnitude is adjusted to stay within the flux hexagon. (a): OVM I (upper boundary). (b): OVM II. (c): six-step [8].	85
5.8	The 18-corner stator flux trajectory in the stationary reference frame [8].	86
5.9	Torque as a function of the flux magnitude and the flux angle for IPMSMs [8].	87
5.10	Torque control methods for DBFC. (a): LUT (open loop). (b): PI regulator (closed loop). (c): hybrid solution [8].	88
5.11	Torque LUT data in the motoring mode [8].	88
5.12	MI and R_ψ at the borders of the different regions of operation. The constant values shown in this figure are calculated while neglecting the inverter's voltage drop and the stator resistance [8].	90
5.13	(a): ψ_R , (b): the shrinking flux hexagon, and (c)-(g): the feasible flux trajectories (yellow) at different rotor speeds. The torque and MTPA-flux are constant ($T_{em}^* = cte$) [8].	91
5.14	Calculation of the feasible flux command (applies to the linear, OVM I, OVM II, and six-step regions). “C” is a point on the circle and “H” is a point on the hexagon. (a): $ OC > OH $. (b): $ OC < OH $ [8].	92
5.15	(a): obtained average flux magnitude compared to the commanded flux (normalized to ψ_R) in the different operating regions. (b): the LUT data needed to achieve a constant average flux magnitude in OVM II. (c): a linear relationship between the commanded flux and the obtained average flux is achieved with the help of the LUT in (b) [8].	93

5.16 Optimal flux vector (red) selection in the linear region (a) and in six-step (b).	94
5.17 Length of the hexagon's segment (C) as a function of the commanded flux angle ($\theta_{\psi*}$).	94
5.18 (a): PWM insertion at the flux hexagon's corners to properly track the reference flux trajectory. (b): zoomed-in view. (c): The calculated duty cycles.	95
5.19 Block diagram of the proposed DBFC controller operating in the linear region, OVM I, OVM II, and six-step. Torque controller (green). ψ_R (purple) and ψ_{MTPA} (tan) calculation. Reference flux vector (orange) and voltage vector (red) calculation. Flux observer (blue). Time-optimal torque controller (pink). Current limiter (yellow) [8].	97
5.20 Simulation results showing the torque, flux, current, and voltage for a step command in torque ($T_{em}^* = 0 \rightarrow 200 \text{ Nm}$) in the linear region. (a)-(d): DB-DTFC. (e)-(h): DBFC. The speed is 4000 min^{-1} . $V_{dc} = 640 \text{ V}$. $T_s = 100 \mu\text{s}$ [12].	98
5.21 Simulation results showing the steady-state operation with DBFC at distinct modulation indices in the linear, OVM I, OVM II, and six-step region, with the help of the predefined flux trajectories. The flux angle command is constant ($\delta_{dq}^* = 1.5 \text{ rad}$). The speed is 10000 min^{-1} . $V_{dc} = 640 \text{ V}$. $T_s = 50 \mu\text{s}$.	99
5.22 Simulation results showing the torque, flux magnitude, and currents of the flux trajectories in Fig. 5.21 for a constant flux angle command ($\delta_{dq}^* = 1.5 \text{ rad}$). 100	
5.23 Simulation results showing the torque step responses ($T_{em}^* = 0 \rightarrow 0.85 \text{ p.u.}$) in six-step for (a),(c): $\hat{\psi}_{pm} = \psi_{pm}$ and (b),(d): $\hat{\psi}_{pm} = 1.1\psi_{pm}$ using the three torque control methods in Fig. 5.10. (c),(d): estimated flux angles. The speed is 0.29 p.u. $T_s = 100 \mu\text{s}$. $K_p = 0.0001 \text{ rad/Nm}$. $K_i = 0.1 \text{ rad/Nm/s}$ [8]. 101	
5.24 Experimental results showing the (a) torque, (b) current, (c) flux, and (d) switching frequency for an increasing speed and with a continuous transition from the linear region to six-step. The current limit is set to 420 A [12]. 102	
5.25 Experimental results showing the flux (blue), voltage (yellow), and current (brown) trajectories, in addition to the phase voltages (red), the duty cycles for phase "a" (purple), and the estimated torque (green) for the different time instants in Fig. 5.24 (c) [12].	104
5.26 Experimental results showing the (a) torque, (b) current, (c) flux, and (d) switching frequency for an increasing torque setpoint using DBFC. The speed is 8000 min^{-1} [12].	105
5.27 Experimental results showing the (a) speed, (b) torque, (c) current, (d) flux, and (e) modulation index, for a speed ramp covering the transition region. The torque command is $T_{em}^* = 0.68 \text{ p.u}$ [8].	106
5.28 Experimental results showing the measured line voltage (blue) and phase current (yellow) for the different operating points in Fig. 5.27 (b) [8].	107
5.29 Experimental results showing the flux (blue), voltage (yellow), and current (brown) trajectories, in addition to u_α^* (red), and the estimated torque (green) for the different operating points in Fig. 5.27 (b) [8].	108

5.30 Experimental results showing the (a) measured phase current, and (b) the corresponding harmonic spectrum, for different load conditions at a constant speed (0.82 p.u.) [8].	109
5.31 Experimental results showing the (a) torque, (b) flux angle (δ_{dq}^*), (c) current, (d) flux magnitude, (e) switching frequency, and modulation index, for an increasing torque command ($T_{em}^* = 0 : 0.042 : 0.68 \text{ p.u.}$) at a constant speed (0.42 p.u.) [8].	110
6.1 Simulation results showing the (a): torque, (b): flux magnitude, (c)-(d): flux and current trajectories in the synchronous reference frame (f_{dq}), (e): flux angle, and (f)-(u): flux trajectory in the stationary reference frame ($f_{\alpha\beta}$) during the transient state for a step command in torque ($T_{em}^* = 0 \rightarrow 0.51 \text{ p.u.}$). The speed is $0.47 \text{ p.u. } T_s = 100 \mu\text{s}$ [8].	115
6.2 The transient flux trajectory (yellow) from an initial steady state (A) to a final steady state B for optimal-time control [8].	116
6.3 Simulation results showing the torque, flux, and current for step command in torque ($T_{em}^* = 0.20 \rightarrow 0.51 \text{ p.u.}$). ①: unoptimized transient flux trajectory. ②: $n = 4$. The speed is $0.47 \text{ p.u. } T_s = 100 \mu\text{s}$ [8].	118
6.4 Simulation results showing the torque, flux, and current for step command in torque ($T_{em}^* = 0.20 \rightarrow 0.51 \text{ p.u.}$). ③: TOC, $n = n_{opt} = 7$. ④: $n = 9$. The speed is $0.47 \text{ p.u. } T_s = 100 \mu\text{s}$ [8].	119
6.5 Simulation results showing the transient flux trajectory of Fig. 6.4 ③ at different time instants with successful time-optimal torque control ($n_{opt} = 7$). $T_{em}^* = 0.20 \rightarrow 0.51 \text{ p.u.}$ The speed is $0.47 \text{ p.u. } T_s = 100 \mu\text{s}$	121
6.6 (a): area (dashed) and side (solid) length of the shrinking flux hexagon normalized to those of the volt-sec hexagon, respectively. (b): the relative size of the flux hexagon and the volt-sec hexagon in the volt-sec plane. $T_s = 125 \mu\text{s}$	123
6.7 Operating principle of the time-optimal torque controller for DBFC [8]. . .	124
6.8 Experimental results showing the torque, flux, and current for step command in torque ($T_{em}^* = 0.20 \rightarrow 0.51 \text{ p.u.}$). ①: unoptimized transient flux trajectory. ②: $n = 5$. The speed is $0.47 \text{ p.u. } T_s = 125 \mu\text{s}$ [8].	126
6.9 Experimental results showing the torque, flux, and current for step command in torque ($T_{em}^* = 0.20 \rightarrow 0.51 \text{ p.u.}$). ③: TOC, $n = n_{opt} = 6$. ④: $n = 7$. The speed is $0.47 \text{ p.u. } T_s = 125 \mu\text{s}$ [8].	127
6.10 Experimental results showing the torque, flux, and current information for step command in torque ($T_{em}^* = 0 \rightarrow 0.20 \text{ p.u.}$). ①: unoptimized transient flux trajectory. ②: TOC with $n_{opt} = 6$. The speed is $0.47 \text{ p.u. } T_s = 125 \mu\text{s}$ [8].	129
6.11 Experimental results showing the torque, flux, and current for step command in torque ($T_{em}^* = 0 \rightarrow 0.43 \text{ p.u.}$). ①: unoptimized transient flux trajectory. ②: TOC with $n_{opt} = 4$ and an integer number of optimal steps. ③: TOC with $n_{opt} = 4$ and a non-integer number of optimal steps. The speed is $0.71 \text{ p.u. } T_s = 125 \mu\text{s}$ [8].	131

6.12 Experimental results showing the torque, flux, and current for step command in torque ($T_{em}^* = 0 \rightarrow 0.27$ p.u.). ①: unoptimized transient flux trajectory. ②: TOC with $n_{opt} = 3$. The speed is 1 p.u. $T_s = 125\mu s$ [8]. . . . 132

List of Tables

3.1	Comparison between the conventional and the simplified DB-DTFC algorithms.	49
3.2	Quantitative comparison between the SRC and the CVC solutions in FW II at 17000 min^{-1} and $ \psi_{dq} = 0.045\text{ Vs}$ [10].	53
3.3	Effect of the iron loss on the current setpoint using CVC at a high and a low state of charge of the battery.	55
4.1	Main factors affecting the flux estimation accuracy.	65
4.2	Operating points tested in the measurement of Fig. 4.8.	72
4.3	Factors affecting the accuracy of the Gopinath flux linkage observer in the different operating regions (“X” has a higher influence than “x”).	76
5.1	Summary of the different torque control methods for DBFC	89
6.1	Summary of the results in Fig. 6.3 and Fig. 6.4.	122
6.2	Summary of the simulation and experimental results in Fig. 6.3, 6.4, 6.8, and 6.9.	128
A.1	Comparison between the DBFC and the DB-DTFC controllers presented in this thesis.	142

Nomenclature

Symbols

v	Stator voltage	[V]
i	Stator current	[A]
ψ	Flux linkage	[Vs]
T_{em}	Electromagnetic torque	[Nm]
ω_{rm}	Mechanical angular speed of the rotor	[rad/s]
ω_r	Electrical angular speed of the rotor	[rad/s]
n_{rm}	Mechanical angular speed of the rotor (revolutions per minute)	[min ⁻¹]
L	Inductance	[H]
ψ_{pm}	Permanent-magnet flux linkage	[Vs]
R_s	Stator resistance	[Ω]
R_i	Iron-loss resistance	[Ω]
P	Number of poles	
V_{dc}	Dc-link voltage	[V]
I_{dc}	Dc-link current	[A]
ψ_R	Circumradius of the flux hexagon	[Vs]
MI	Modulation index	
R_ψ	Average flux magnitude normalized to ψ_R	
V_1	Peak magnitude of the fundamental phase voltage	[V]
f_1	Fundamental electrical frequency	[Hz]
f_s	Switching frequency	[Hz]
N_p	Pulse number	
θ	Angle referred to the $\alpha - axis$	[rad]
δ	Angle referred to the $d - axis$	[rad]
θ_r	Rotor position	[rad]
t	Time (continuous)	[s]
T_s	Sampling time	[s]
k	Current sample (discrete)	

K_p, K_i	Coefficients of the proportional and integral terms	
$S_{a,b,c}$	Switching states of the three-phase voltage source inverter	
ΔT_{em}	Change in the electromagnetic torque	[Nm]
M	Slope of the differential torque line	
B	q-intercept of the differential torque line	[Vs]
$-x, -y$	Flux circle center coordinates	[Vs]
n_{opt}	Optimal number of time steps to achieve TOC	
P_{cu}	Copper losses	[W]
P_i	Iron losses	[W]
f_{abc}	Stationary three-phase reference frame	
$f_{\alpha\beta}$	Stationary two-phase reference frame	
f_{dq}	Synchronous two-phase reference frame	
j	Unit imaginary number	
(\circledast)	Operating point ($x \in \mathbb{N}^*$)	
\hat{x}	Estimated parameter	
x^*	Commanded variable	

Acronyms and Abbreviations

AC	Alternating current
CM	Current model
CO	Current observer
CVC	Current vector control
DB-DTFC	Deadbeat-direct torque and flux control
DBFC	Deadbeat flux vector control
DC	Direct current
DSC	Direct self control
DTC	Direct torque control
EV	Electric vehicle
FO	Flux observer
FW	Flux weakening
HIL	Hardware in the loop
IGBT	Insulated-gate bipolar transistor
IPMSM	Interior permanent magnet synchronous machine
LPF	Low-pass filter
LUT	Lookup table
MOSFET	Metal–oxide–semiconductor field-effect transistor

MTPA	Maximum torque per ampere
MTPF/V	Maximum torque per flux/voltage
MTPL	Maximum torque per loss
OPP	Optimized pulse pattern
OVM	Overmodulation
PI	Proportional–integral controller
PWM	Pulse width modulation
RMS	Root mean square
SRC	Square root condition
SVM	Space vector modulation
TOC	Time optimal control
VATC	Voltage angle torque control
VM	Voltage model